4-28-2009

Experimental Characterization of Induction Electrohydrodynamics for Integrated Microchannel Pumping

Brian D. Iverson
Purdue, bdiverson@byu.edu

S V. Garimella
Purdue Univ, sureshg@purdue.edu

J. Micromech. Microeng. **19** (2009) 055015 (12pp) doi:10.1088/0960-1317/19/5/055015

Experimental characterization of induction electrohydrodynamics for integrated microchannel pumping

Brian D Iverson and Suresh V Garimella

Cooling Technologies Research Center, School of Mechanical Engineering and Birck Nanotechnology Center, Purdue University, 585 Purdue Mall, West Lafayette, IN 47907, USA

E-mail: sureshg@purdue.edu

Received 14 January 2009, in final form 15 March 2009
Published 28 April 2009
Online at stacks.iop.org/JMM/19/055015

Abstract

Microscale fluid flow using traveling-wave induction electrohydrodynamics is demonstrated. A three-phase traveling-wave device fabricated for the experiments provides a temporally and spatially varying electric field which helps induce ions in a fluid that is subjected to a temperature gradient. These ions are moved as the traveling wave propagates, resulting in a drag force being exerted on the surrounding fluid. Repulsion-type electrohydrodynamic flow is visualized in a microchannel of depth 50 μm, and results are presented in terms of velocity measurements using particle image velocimetry. The effects of voltage, traveling-wave frequency and the addition of externally applied heat are demonstrated and heat transfer capabilities of the micropump are discussed.

(Some figures in this article are in colour only in the electronic version)

1. Introduction

Microfluidic platforms to facilitate the transport of heat and mass have received much attention in recent years [1–3]. Microchannels have gained acceptance in the thermal community as a viable option for electronics cooling [4, 5] as they offer the ability to increase power dissipation while also maintaining a small form factor. Contact and spreading resistances at different interfaces in the package can be reduced or even eliminated by integrating microchannels directly on the backside of common flip-chip designs. Further, by using liquid cooling, the heat-generating and heat-dissipating components can be separated (see figure 1(*a*)), allowing the convective surface area on the air side to be unconstrained by the microprocessor area [6]. Solutions which integrate micropumps directly into the microchannels have the potential for enabling microchannel cooling in electronic systems while also reducing cost and size requirements.

Additionally, the development of cell analysis tools has recently targeted microfluidic devices since they can be used to sample, trap, separate, sort, treat and analyze cells [7, 8]. Microfluidic devices offer many benefits for biological handling and analysis. For example, reducing device size through microfabrication reduces sample requirements and reagent volumes while also enabling disposable systems, which is important for sterility. The use of a closed system also protects the operator from chemical exposure, reduces contamination and eliminates human intervention and error [9]. Parallel operations, integration of multiple functions and short transition lengths also reduce analysis times. However, for microfluidic devices to capitalize on all of the above benefits, integration of the fluid pumping mechanism is imperative. Early microfabricated cell-sorting devices have used electroosmotic flow as the driving mechanism, but suffer from low sample throughput [10]. An increased throughput has been achieved using pressure-driven alternatives, but at the expense of removing the pumping mechanism from the chip level [9, 11]. Regardless, the target flow rates for pumping biological materials are typically much lower than for convective cooling, allowing reduced demands on pump operating conditions (such as voltage and power consumption) to obtain the desired range of fluid flow rates.

Recent reviews of micropumping mechanisms are available in [1–3, 12, 13]. Traveling-wave induction electrohydrodynamics (EHD) is one method of flow actuation in which a gradient in the electrical properties of the fluid

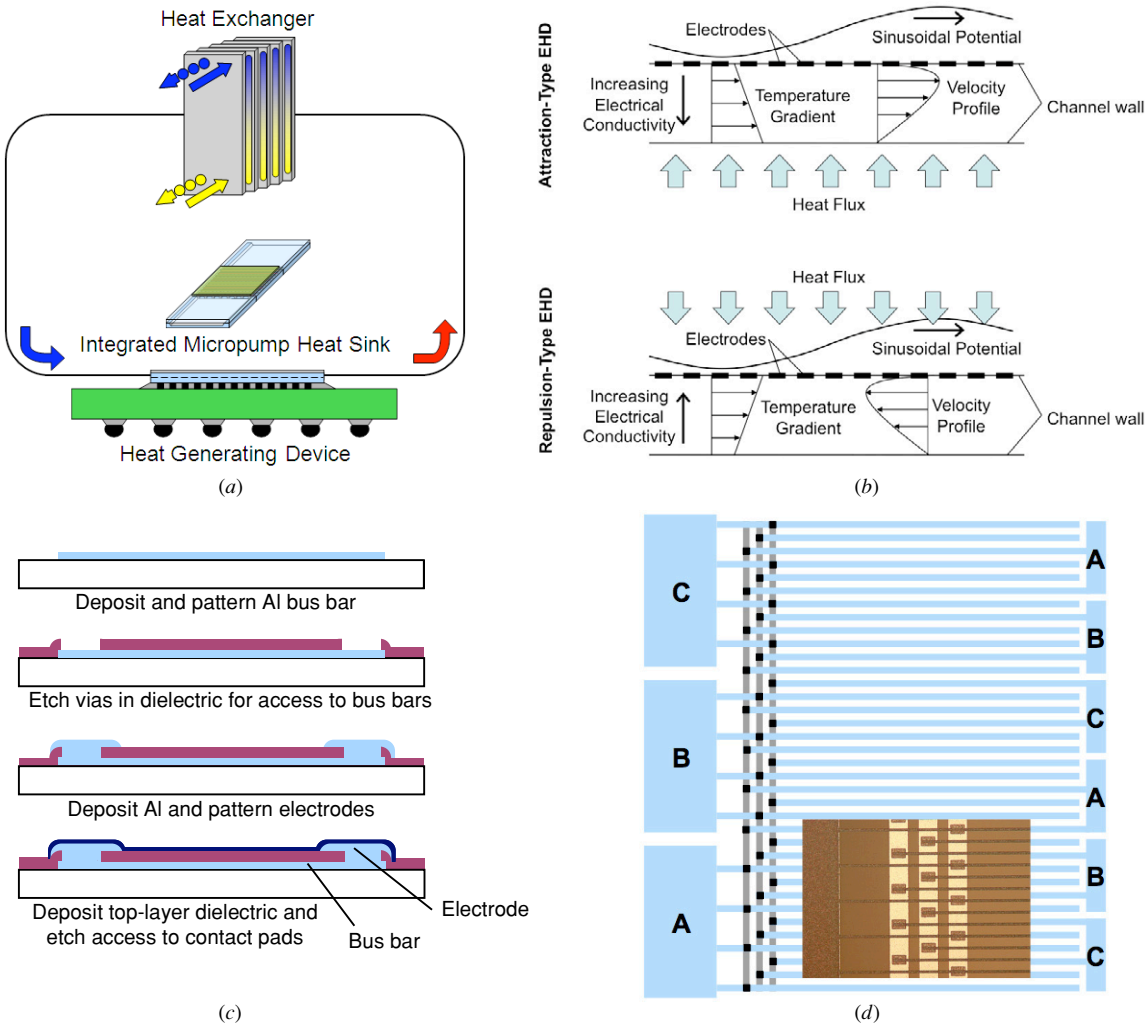

Figure 1. Schematic diagrams of (*a*) a microchannel-integrated micropump system for cooling, (*b*) principles of attraction- and repulsion-type EHD, (*c*) traveling-wave device cross-section (*d*) and layout of a completed three-phase device with micrograph inset.

is established through the depth of the microchannel in response to a thermal gradient (figure 1(*b*)). Ions are induced in the electric field near the electrode boundary that relax in time but can be manipulated with a traveling-wave voltage boundary condition. Although EHD has been studied for many years [14–18], it has recently emerged as a potential driving mechanism for micropumps due to its miniaturization potential [19, 20]. Further, EHD pumps have the ability to pump a variety of liquids for applications in various research fields [21]. A particular advantage of these pumps is that for traveling-wave induction EHD pumps, only minor modifications are necessary to enable pumping of different types of liquids including a change in frequency of excitation [22].

On one boundary of the channel for traveling-wave EHD-induced flows, a sinusoidally varying voltage provides the spatially and temporally varying electric field necessary for ion induction and translation, respectively. The temperature gradient (across the channel depth) establishes the gradient in electrical properties necessary for ion induction. This temperature gradient can be applied in either direction and dictates the attraction or repulsion of the ions (and resulting fluid flow direction) with respect to the direction of the traveling wave. In attraction-type induction EHD, the fluid at the lowest temperature which has the lowest electrical conductivity is closer to the electrodes where the most intense electric field is present in the microchannel (figure 1(*b*)). The fluid follows the traveling potential wave in the same direction since the induced charges are 'attracted' toward the traveling wave. In the case of repulsion-type induction EHD, the region of high electrical conductivity also has a high electric field resulting in charges being repelled in a direction opposite to that of the traveling wave (see figure 1(*b*)).

Melcher and Firebaugh [15], in an early EHD model, used the electric shear approach to calculate the flow profile due to induction EHD by neglecting the time and space variation in induced charge density. Later models have considered a similar approach using the electric shear stress but have included developing flow as well [16, 17].

Numerical schemes have been presented for traveling-wave-induced electrothermal fluid flows in which material selection and device geometry play an important role in determining driving forces [23]. The effects of illumination methods used for experimental characterization, and of

Table 1. Layer composition for processed wafers (all values in μm).

Layer	Material	Wafer 1	Wafer 2	Wafer 5	Wafer 8
1	Evaporated Al	0.50	0.50	0.50	0.50
2	PECVD Oxide	0.60	0.67	0.60	0.78
3	Sputtered Al	∼0.5	∼0.5	∼0.5	∼0.5
4	PECVD Oxide	0.17	0.17	0.20	0.20

Joule heating on temperature gradients in electrothermal flows, have also been investigated [24]. Temperature field-controlled induction EHD, in which the temperature gradient is controlled using Peltier elements, has also been discussed [25]. Flow velocities were shown to increase by increasing the temperature-dependent conductivity gradient for relatively low applied voltages. A force–density approach, which can predict the induced charge density as a function of both space and time, was used to numerically model induction EHD [26] and was employed to illustrate the effects of physically discretized traveling waves [27].

Experimental evidence of traveling-wave EHD flows has been reported but is generally limited to the electrical and hydrodynamic aspects of the induced flow. The current study presents experimental evidence of the impact of thermal conditions on the resulting fluid flow. The design and experimental characterization of microscale, traveling-wave induction EHD devices operating in a fluid repulsion mode are presented, with experimental results reported in terms of average velocities. Effects of traveling-wave voltage and frequency on EHD-induced flows are experimentally investigated. The increase in fluid velocity with an increase in temperature difference across the channel depth is experimentally demonstrated. A comparison of the experimental results with a previously developed numerical model is provided. Finally, the heat transfer capabilities of the flows generated by the micropump are estimated.

2. Micropump fabrication

An EHD micropump that employs a traveling-wave voltage boundary condition has been fabricated. The device comprises four distinct layers that have been surface-micromachined on a Pyrex wafer: a bus bar sub-layer, a passivating dielectric film, an array of parallel electrodes and a top-layer dielectric. Fabrication was conducted at the Birck Nanotechnology Center of Purdue University and a brief description of each layer now follows. A summary of the device geometry and properties is provided in tables 1 and 2.

Three parallel bus bars representing each phase of the traveling wave were deposited by evaporating ∼0.5 μm of Al with a CHA e-beam evaporator on a Pyrex 7740 substrate. The metal layer was then patterned by wet-etching areas exposed after AZ 1518 photolithography (see figure 1(*c*)).

The second layer comprises a PECVD oxide dielectric film used to separate the electrode array and the bus bar layer. A blanket layer (0.60–0.78 μm thick, table 1) of oxide was deposited directly on top of the bus bars using a BenchMark Axic PECVD system. Vias were etched into the dielectric using CF_4 and C_4F_8 in an RIE process and patterned using AZ 1518 as a mask. These via windows allow the electrical contact between the electrodes and the underlying bus bars (figure 1(*c*)). Each phase is separated by a distance equal to the dielectric film thickness.

Table 2. Device, traveling-wave and flow visualization parameters for induction EHD experiments.

Parameter	Value
Device parameters	
Substrate material	Pyrex 7740
Substrate thickness (μm)	500
Electrode width (μm)	8
Electrode spacing (μm)	16
Pumping section length (cm)	1
Pumping section width (cm)	0.5
Channel depth (μm)	50
Traveling-wave parameters	
Wavelength (μm)	72
Phases	3
Flow visualization parameters	
Particle mean diameter (μm)	0.86
Excitation wavelength (nm)	542
Emission wavelength (nm)	612
Volume concentration of particles for PIV	0.01% (v/v)
Microscope objective	50×
Pixel width (1024 × 1024 frame) (μm)	0.3401

A second metallization step using a Perkin Elmer sputter deposition system is used to deposit an ∼0.5 μm Al layer on top of the dielectric thin film in a conformal fashion. The conformal nature of sputtering is especially important here in order to provide good step coverage across via openings. Since aluminum oxide can form on the underlying evaporated Al, a brief Ar sputter-etch was performed under vacuum before moving the Al target in place for deposition. The sputter-deposited metal layer was patterned by wet-etching areas exposed after AZ 1518 photolithography as before. Although the same Al etch recipe is used for etching both e-beam evaporated and sputter-deposited metals, etch times for the sputtered metal layer were approximately half those for the e-beam evaporated metal layer. The electrodes cover roughly a 1 cm^2 area and can be activated by a number of contact pads on both ends of the electrodes (figure 1(*d*)). The nominal electrode width and spacing are 8 μm and 16 μm, respectively. Thus, a series of approximately 417 electrodes (139 wavelengths) span the length of the 1 cm long pumping region. The reduction of electrode pitch by using microfabrication techniques such as photolithography to define small features on this order also helps reduce the applied voltage requirement to achieve high electric fields useful for pump operation.

A final top-layer dielectric was deposited over the electrical network to protect the metal electrodes from metal migration and corrosion. Access windows to the contact pads were etched in the top-layer dielectric using the RIE process described above to accommodate the electrical actuation of the phases. The final completed device is shown in figure 1(*d*) and the inset.

The electrode array responsible for supplying the electric field for induction EHD is surface-micromachined on a single

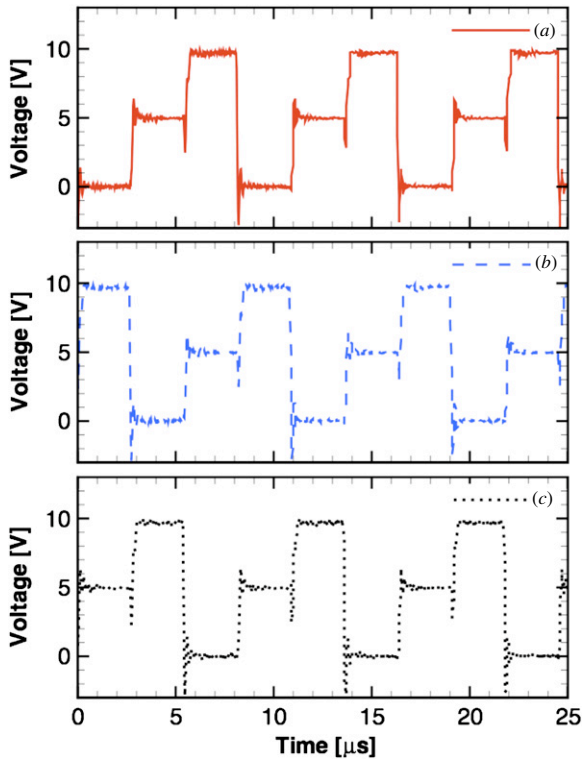

Figure 2. Measured three-phase signal applied to the electrode array illustrating the step change in voltage and phase shift between phases (*a*), (*b*) and (*c*).

die in this manner, and this die could be used as the physical lid of a microchannel array. In this manner, the traveling-wave boundary could be integrated directly into the microchannels used for convective cooling of electronic chips. While anodic bonding is commonly used as an attachment method to Si substrates, the roughness caused by the surface topography of the electrodes makes this method ineffective. Glass frit bonding and other thin-film adhesives may be used for attachment. For the experiments in this work, a provisional solution for bonding is used.

3. Experimental conditions

This section outlines the experimental conditions for the applied three-phase signal and the properties of the fluid used in the traveling-wave induction EHD experiments.

3.1. Three-phase signal

The output signal applied to the three-phase electrode array is shown in figure 2. A Kepco dc voltage supply and BNC 555 pulse generator were used to supply the desired voltage and frequency to a custom three-phase pulse generator developed for an earlier project and described elsewhere [28]. This custom three-phase pulse generator outputs a signal that switches between 0, half and full value of the input voltage V at the frequency set by the BNC 555 pulse generator. The three phases of the custom three-phase pulse generator are connected to the large contact pads on the left side of the device (as shown in figure 1(*d*)) and transient voltage data collected by probing three of the small contact pads on the right side of the device. In this manner, interference between the three phases on the device could be observed across the electrode array. Figure 2 illustrates the signal provided to the electrodes as a function of time for input settings of 10 V and 122.1 kHz, as viewed by an oscilloscope. The three phases show the appropriate, desired levels of voltage as a function of time.

3.2. Fluid properties

A low-concentration KCl solution (2.18×10^{-5} M, electrical conductivity $\sigma_{\text{nominal}} = 3.56\ \mu\text{S cm}^{-1}$ at 25 °C) was selected as the working fluid for the micropump. The flow is visualized by seeding this liquid with small fluorescent polystyrene particles (Duke Scientific, 0.86 μm mean diameter, table 2) that fluoresce in response to light at a wavelength of 542 nm and emit at 612 nm. The particles used for visualization come suspended in a 1% (w/w) concentrated solution and are diluted in the KCl solution to a 0.01% (v/v) concentration. The fluid electrical conductivity was measured before and after suspending the fluorescent polystyrene particles in the KCl solution. On average, the fluid electrical conductivity increased from approximately 4 $\mu\text{S cm}^{-1}$ to 6 $\mu\text{S cm}^{-1}$ (see table 3) upon addition of the tracer particles. It is possible that the surfactant liquid in which the particles are suspended contributes to this increase in electrical conductivity. The fluid electrical conductivity is also temperature dependent; a 2.2% change in electrical conductivity per °C is assumed for the electrolyte used here [19].

With an applied voltage in contact with an aqueous solution, electrolysis can occur which can introduce bubbles into the fluid domain. In order to estimate the extent of possible electrolysis, the volume of hydrogen and oxygen formation can be calculated by combining Faraday's law of electrolysis [29] with the ideal gas law. By comparing the volume of gas generated to the volume of the pumping chamber, the relative impact of electrolysis can be estimated. For an average fluid conductivity of 6 $\mu\text{S cm}^{-1}$ at room temperature and an applied voltage of 30 V, the fraction of hydrogen gas to liquid volume is approximately 0.1% over a test time period of 3 min. The volume of oxygen would be approximately six times smaller than that of hydrogen. Therefore, the effects of electrolysis are neglected in this work. Moreover, no electrolysis effects were visually observed in the experiments.

3.3. Experimental setup

The experimental setup used for actuating flows using EHD is shown in figure 3. In order to visualize flow velocities through a transparent cover plate, a repulsion-type EHD configuration was selected in which the electrode and heated boundary are both located on the bottom wall of the channel domain. When applying additional heat beyond that due to self-heating, a thin-film polyimide heater (6.35 × 6.35 mm, Minco HK5565R5.3L12E) was attached to the electrode array die on the backside of the quartz to increase the temperature gradient in the fluid. The surface-micromachined electrode

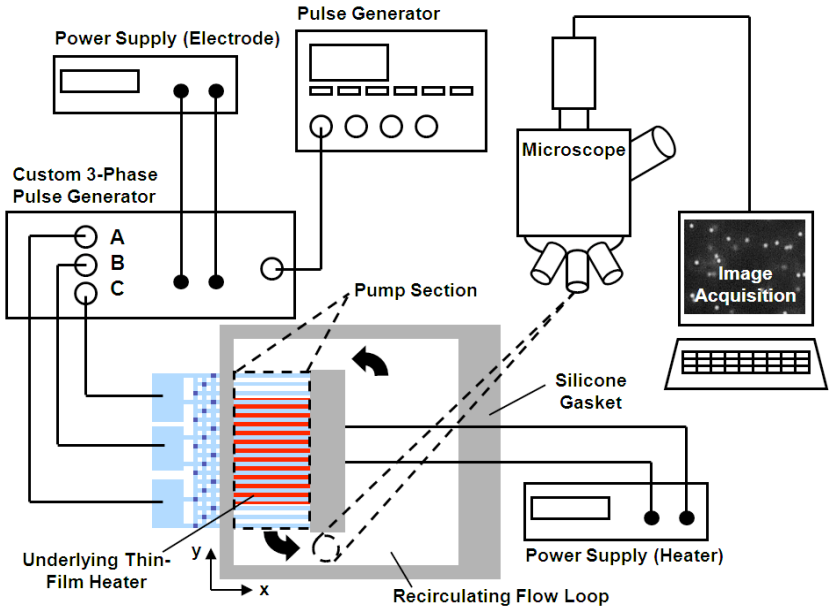

(*a*)

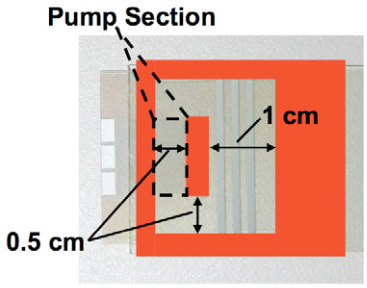

(*b*)

Figure 3. (*a*) Experimental setup for PIV and device characterization (not to scale), and (*b*) instrumented device with the silicone gasket used to form the recirculating channel highlighted.

Table 3. Experimental parameters of the different dies tested.

Parameter	Wafer 2 Die 1	Wafer 5 Die 3	Wafer 5 Die 5	Wafer 8 Die 3
Capacitance between phases (pF)	85–90	80–85	–	80–85
Fluid conductivity (μS cm^{-1})/temperature (°C) (before seeding with fluorescent particles)	3.96/21.2	–	–	3.84/21.4
Fluid conductivity (μS cm^{-1})/temperature (°C) (after seeding with fluorescent particles)	6.27/21.8	6.56/21.8	5.92/21.4	6.30/21.9
Ambient temperature (°C)	21.3	21.4	21.3	21.2

array is on top of the quartz die, interior to the channel. A silicone gasket (Adhesives Research ARclad® 7876, 50.8 μm thickness) with double-sided adhesive was used to attach a glass cover slide to the electrode die and create a recirculating channel flow path which is 50.8 μm deep (as shown in figure 3(*b*)).

The custom three-phase pulse generator is used to electrically activate each of the three phases on the fabricated circuit. With the electrical and thermal boundary conditions established, the flow is visualized by means of the polystyrene seed particles described earlier.

Time-resolved images for particle image velocimetry (PIV) were captured using a microscope with a 50× objective and an attached Photron Ultima APX high-speed camera at 60 fps. The camera can provide a full pixel resolution of 1024 × 1024 at this frame rate; with the 50× objective, the corresponding spatial resolution is approximately 0.34 μm (table 2). For a numerical aperture of 0.5 and an emission wavelength of 612 nm, the depth of field is 3.3 μm and the measurement depth is 12.7 μm. Thus, the measurement depth covers approximately a quarter of the channel depth.

Once the images for PIV analysis were recorded at a location before the fluid enters the pumping section of the flow path, the flow at an opposite location in the flow loop was also observed to verify liquid recirculation in the closed loop and not simply particle motion. Using the images obtained at

a location outside the electrode region ensures that the particle motion was due to induced fluid flow, and not, for instance, by dielectrophoretic motion of the particles alone within the fluid (see figure 3). Further, the flow direction confirms that the flow was indeed repulsion-type EHD as the direction was opposite to that of the traveling-wave direction.

4. Experimental results

Results were obtained for the three-phase traveling-wave device for a range of operating conditions. In cases where no external heating was applied, Joule heating from the electrode array served to establish a temperature difference across the channel depth. For low flow rates, Joule heating is sufficient to cause the desired temperature difference across the channel depth as can be shown from the order-of-magnitude method of Ramos *et al* [30].

A series of 334 images capturing the tracer particle motion were obtained sequentially at 0.05 s increments and used to perform a particle image velocimetry (PIV) analysis using the research software EDPIV (developed at the Institute of Fluid Mechanics at the University of Essen in Germany, Iowa Institute of Hydraulic Research at the University of Iowa and Purdue University [31]). A traditional correlation-based approach was used with a multi-pass interrogation routine and fast Fourier transforms to accelerate the analysis. The velocity fields, as well as the mean velocities, were obtained in this manner. PIV analysis was performed using 100 and 200 sequential frames in addition to the full 334 image set to establish convergence of the solution and ensure accurate results. The results changed by less than 5% when the number of images interrogated was increased from 100 to 200. This difference further decreased to less than 2.5% as the interrogated image set was increased to 334. All velocities reported herein were obtained using the full 334 image set. Further, the standard deviation of the resulting velocity vectors in the 150 mm square interrogation area was less than 10% for all cases.

A sample velocity field of the EHD flow is shown in figure 4. This example case is for a 30.1 V, 122.1 kHz traveling wave with no externally applied heat. As can be seen here, the flow appears uniform over the area with a little difference in neighboring velocity vectors. With the flow visualized at the location indicated in figure 3, very little flow is observed in the y direction as expected.

4.1. Voltage dependence

Figure 5(a) illustrates the dependence of the average fluid velocity on the square of the applied voltage associated with the traveling wave. All data points in figure 5(a) are for a frequency of 122.1 kHz with no external heating. This data set was constructed using results collected from all of the devices presented in tables 1 and 3. An approximately linear relationship between the fluid velocity and the square of the voltage is quite apparent; the scatter is due to differences in test conditions such as fluid conductivity and dielectric layer thickness. Inspection of the analytical approach developed by

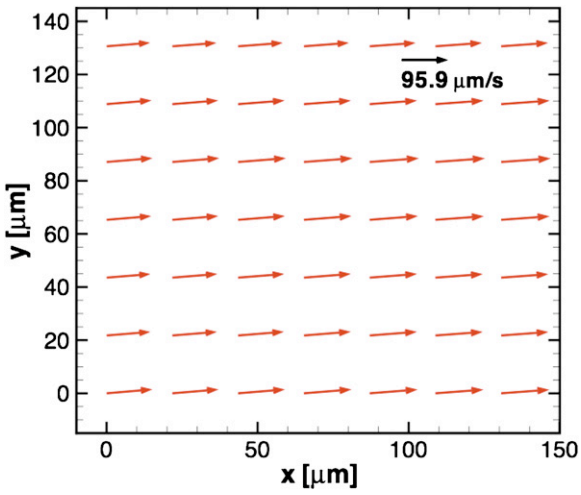

Figure 4. PIV velocity field (average velocity 95.9 μm s^{-1}) generated using repulsion-type induction EHD with die 3 from wafer 8 ($V = 30.1$ V, $f = 122.1$ kHz). The standard deviation in velocity vectors from PIV measurement is less than 10% in all cases. The x–y origin in this plot is arbitrary and the axes only provide a scale. The measurement location is indicated in figure 3.

Melcher and Firebaugh [15] reveals this expected quadratic dependence of velocity on the applied voltage. Thus, despite some scatter, this trend is clearly seen from the cases presented in figure 5(a). The velocities range from 17 to 96 μm s^{-1} as the voltage is incremented from 10 to 30 V.

The expected increase in the temperature difference across the channel depth from greater Joule heating is seen in figure 5(b) which plots the increase in exterior lower-wall surface temperature with the applied voltage for the cases included in figure 5(a). Some of the scatter in the velocities shown in figure 5(a) is also likely due to the scatter in ΔT as indicated in figure 5(b).

4.2. Frequency dependence

Traveling-wave EHD flows are not only dependent on the driving voltage but also on traveling-wave frequency. Figure 6 illustrates the dependence of fluid velocity on traveling-wave frequency, for die 3 from wafer 8. All data points on this plot are for a 10.1 V driving voltage. As the frequency is increased from 10.0 kHz to 49.9 kHz, a distinct increase in velocity is observed that peaks before decreasing monotonically with further increases in frequency.

The peak in velocity may be expected to occur when the traveling-wave frequency corresponds to the charge relaxation time ($f = 1/2\pi\tau$, with charge relaxation time constant $\tau = \varepsilon_r\varepsilon_0/\sigma$, relative permittivity ε_r, permittivity of vacuum ε_0 and electrical conductivity σ) such that the charges are able to fully transit from one electrode to the next without suffering long residence times before the voltages assigned to the electrode array change. If the frequency is lower, induced charges reach their equilibrium position opposite the traveling wave quickly and the tangential shear exerted on the fluid is small. At higher frequencies, on the other hand, the relaxation process inhibits charge from accumulating at the surface, also reducing the shear stress [32]. The upper and lower limits of the

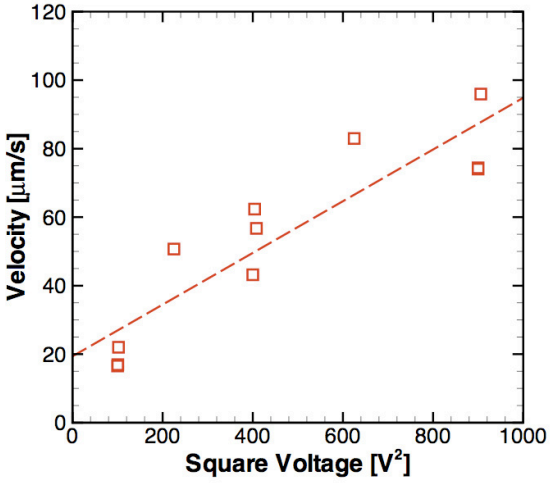

(*a*)

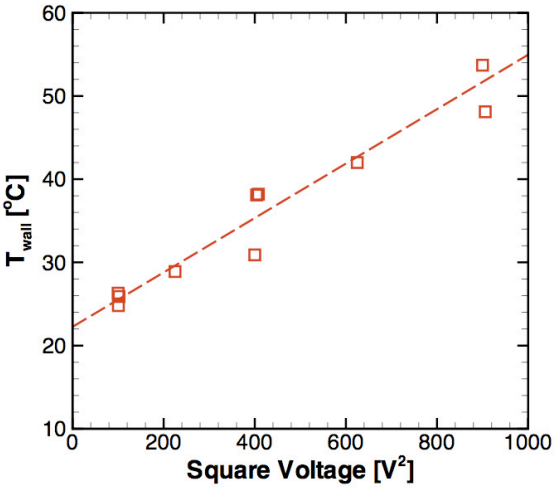

(*b*)

Figure 5. (*a*) Measured PIV velocities generated using repulsion-type induction EHD, and (*b*) exterior lower-wall surface temperature as a function of the square of the applied voltage for the three-phase traveling wave on devices from wafers 2, 5 and 8 (f = 122.1 kHz). Uncertainty in velocity and temperature measurements is ±47% and 2 °C, respectively.

shaded region in figure 6 represent the ideal frequency range (86.3–141.5 kHz) using the fluid conductivity values measured before and after suspending the microspheres in the fluid, respectively, assuming a dielectric constant of 80. The actual peak in velocity occurs at a somewhat lower frequency than might be expected based on the charge relaxation time. This is consistent with the experimental results obtained by Fuhr *et al* who obtained peak velocities near or below the frequency based on the charge relaxation time [22].

Figure 6 also shows the exterior lower-wall temperature as a function of frequency at a 10.1 V peak voltage. The wall temperature appears to increase with frequency although the temperature change associated with frequency change is relatively small (<3.5 K). Despite the increase in lower-wall temperature and the corresponding increase in ΔT across the channel depth, the peak in velocity is observed at an

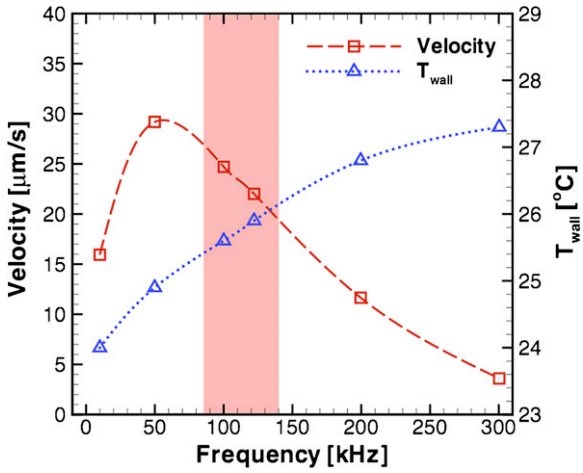

Figure 6. Measured PIV velocities generated using repulsion-type induction EHD and exterior lower-wall surface temperature as a function of the frequency of the applied three-phase traveling wave on a device from wafer 8 (V = 10.1 V). Uncertainty in velocity and temperature measurements is ±47% and 2 °C, respectively.

intermediate frequency. Thus, the velocity peak in figure 6 is clearly dominated by frequency.

4.3. Effect of applied heat

The experimental results reported thus far were generated using the temperature difference across the channel depth established by Joule heating in the device. An external heat source can be used to increase this ΔT and thereby increase the gradient in fluid properties and corresponding fluid velocity. In the next set of experiments, external heat was applied to the device and allowed to reach a steady-state temperature before the traveling wave was imposed. Further, it was verified that there was no fluid motion until the traveling wave was applied even with the applied heat activated. Figure 7 illustrates the impact of external heating on the measured fluid velocity; the lower-wall temperature is also listed for each data point. The data point at $P_{\text{heater}} = 0$ W is the reference case with no external heating. The remaining cases represent increased heat dissipation in the thin-film heater attached to the exterior lower wall. All cases are driven by a 10.0 V, 122.1 kHz traveling wave.

As the applied heat increases, a corresponding increase in measured velocity is observed owing to a stronger thermal gradient in the channel depth. In fact, for the modest increase in externally applied heat dissipation from 0 to 0.3 W, a 49.6% increase in velocity is achieved.

4.4. Power

In order to determine the amount of power required to generate a certain velocity of fluid flow, the pressure drop experienced by the fluid at that velocity is required. The pressure head generated by the micropump is evaluated using a numerical model of the channel using an imposed average velocity at the inlet. The channel is 0.5 cm wide on three sides of the recirculating flow and 1 cm wide on the fourth side (figure 3(*b*)). The channel depth is 50 μm, and the fluid

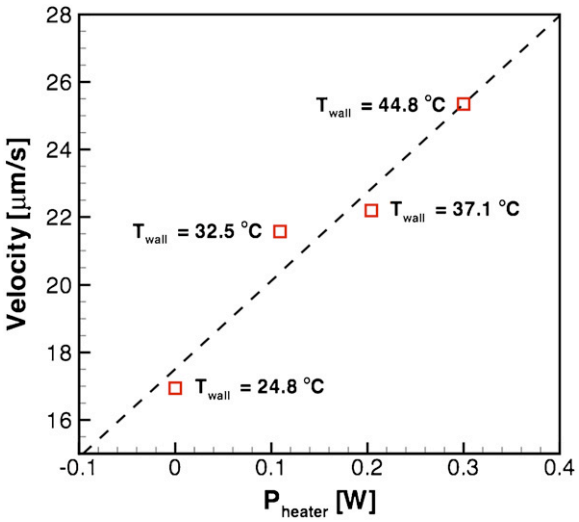

Figure 7. Measured PIV velocities generated using repulsion-type induction EHD as a function of the external applied heating on the lower boundary using a device from wafer 5 ($V = 10.0$ V, $f = 122.1$ kHz). Uncertainty in velocity and temperature measurements is ±47% and 2 °C, respectively.

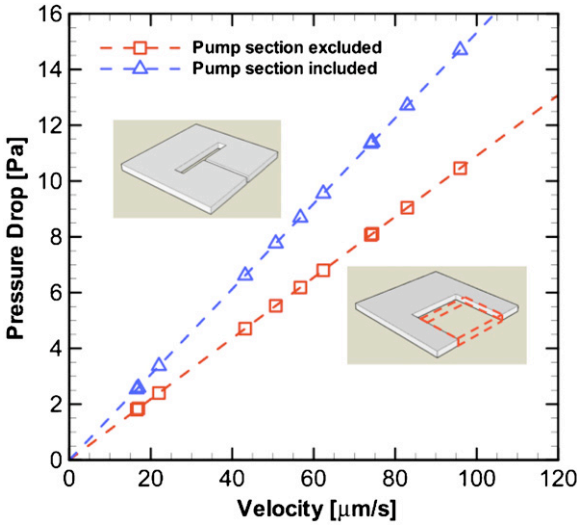

Figure 8. Numerically computed values of pressure drop in the recirculating channel as a function of velocity for the experimentally obtained velocity measurements of figure 5(*a*) with and without the pumping section included as indicated by the schematic insets.

properties for the numerical computation are density, $\rho = 998$ (kg m^{-3}) and dynamic viscosity, $\mu = 1.003 \times 10^{-3}$ (kg m^{-1} s^{-1}) (see also parameters in table 2). Mesh independence was ensured with a less than 1% variation in pressure drop observed for finer meshes.

Two alternative domains were considered in evaluating the pressure drop—one which includes the 1 cm long active pumping section identified in figure 4, and the other which excludes the pumping section. The Δp values and fluid power (pressure drop × volume flow rate) are numerically calculated over the 20–100 μm s^{-1} average velocity range obtained from the experimental measurements. The resulting pressure drop for all the velocities reported in figure 5(*a*) is shown as a function of flow velocity in figure 8. The pressure drop is larger

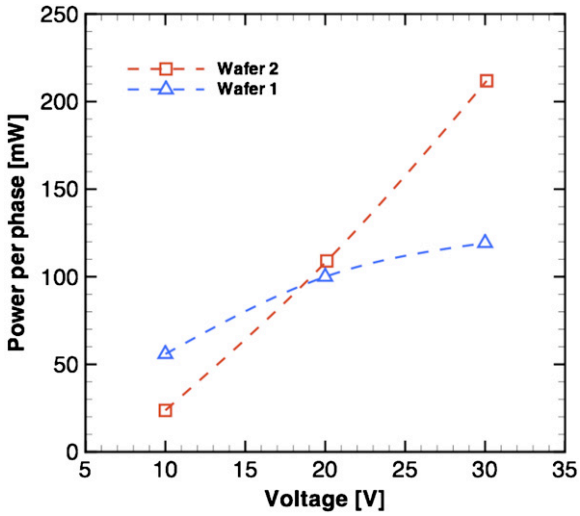

Figure 9. Measured power for an input signal of 122.1 kHz over a range of applied voltages as supplied to one phase of a three-phase traveling-wave device.

when the active pumping section is included, as expected, and ranges from 2 to 15 Pa for these low flow rates. The fluid power for this range of pressure drop and velocities varies from 1.1×10^{-11} to 38.3×10^{-11} W.

To estimate the power required to operate the traveling-wave EHD pump, the voltage and current supplied to the device are needed. A resistor is placed in series with the device and the time-varying voltage signal is measured across the resistor using an oscilloscope (10 MΩ, 15 pF probes). The channel top wall consisting of an ITO-coated slide was passivated using an ∼200 nm film of PECVD oxide and grounded for the power measurement. Using the known resistor value (27 Ω) and the voltage differential obtained by subtracting the voltage signals, the current can be determined as a function of time as $\Delta V(t)/R$. The power consumption P is calculated by integrating the time-varying voltage input $V(t)$ and current $I(t)$ over the time period t of the measurement signal as follows:

$$P = \frac{1}{t}\int_0^t V(t')I(t')\,\mathrm{d}t'. \quad (1)$$

The time-varying voltage signals were measured over five or more wavelengths of the traveling wave while the device was operating at steady state. These data were then imported into MATLAB for numerical integration. Figure 9 illustrates the average amount of power supplied per phase for three-phase traveling-wave devices from wafers 1 and 2 over a range of applied voltages. All measurements in this figure were obtained at a frequency of 122.1 kHz. As implied by the values in figure 9, a three-phase device would consume roughly 75–650 mW over a voltage range of 10–30 V when activating all three phases for traveling-wave induction EHD.

5. Numerical model comparison

To address some of the limitations of earlier models, a numerical model for induction EHD has been developed [26, 27]. This model has been validated against an

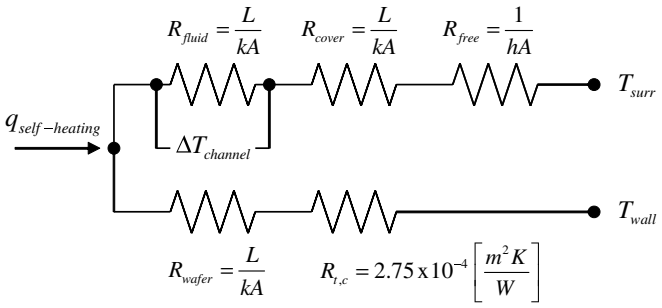

Figure 10. 1D resistance network for determining the temperature difference across the channel depth.

early analytical model by Melcher and Firebaugh [15]. Modeling induction EHD involves simultaneously addressing the presence of electrical, fluid, and thermal conditions imposed on the problem domain. Figure 1(*b*) illustrates a microchannel with these imposed conditions for both attraction- and repulsion-type EHD. In the computations here, we consider repulsion-type EHD in a microchannel to simulate the experimental cases presented.

We assume a 2D representation of the 50 μm deep, 0.5 cm wide and 1 cm long channel encompassing the pumping section, in view of the large channel width-to-depth ratio. The finite element software package FIDAP [33] is used to numerically model the transport equations outlined in [27] for the 2D parallel-plate channel. At each time step, the voltage assigned to the discrete electrodes along the boundary (used to provide a spatially varying, sinusoidal voltage along the wall) is updated using user-defined functions. Discretization of the boundary is discussed in detail in [27]. Both voltage and charge distributions are tracked throughout the calculation in response to the changing voltage boundary condition. Increasing the node count from 70 749 to 129 129 resulted in a difference of less than 5% in the velocity, providing satisfactory mesh independence. Therefore, the coarser mesh was used in the following computations. Further discussion of the validity of this model is provided in [34].

The numerical model was developed with the temperature difference across the channel and associated temperature-dependent properties being provided as inputs. In order to estimate the actual temperature difference across the channel depth, a 1D resistance network was used and is illustrated in figure 10. This network represents the case when the device is self-heated. As heat is generated in the device, the heat can flow either down through the wafer (where a thermocouple is instrumented to read the lower wall temperature) or up across the fluid thickness which would define ΔT. The resistances to the heat flow in either direction are defined in figure 10. Numerical inputs for evaluating these resistances are provided in table 4.

Assuming that the dominant component of power dissipation goes to self-heating (as indicated by the small amount of fluid power generated), we can use the power values from figure 9 as an approximation for the amount of heat entering the 1D resistance network. For the 635 mW power input required for the 30 V case and a wall temperature

Table 4. Parameters used in evaluating the temperature difference across the channel depth using the 1D resistance network of figure 10.

Parameter	Value
Air	
Ambient temperature (°C)	21.5
Coefficient of thermal expansion, β (1/K)	3.33×10^{-3}
Kinematic viscosity, ν (m^2 s^{-1})	15.89×10^{-6}
Thermal diffusivity, α [m^2 s^{-1}]	22.5×10^{-6}
Glass cover	
Thickness (mm)	1
Thermal conductivity (W m^{-1} K^{-1})	1.4
Fluid	
Thickness (μm)	50
Thermal conductivity (W m^{-1} K^{-1})	0.6
Pyrex wafer	
Thickness (μm)	500
Thermal conductivity (W m^{-1} K^{-1})	1.4

Table 5. Parameters used in comparing predictions from Melcher and Firebaugh's analytical model [15] and the current numerical model [26, 27] with the experimentally obtained velocities of figure 5.

Parameter	Value
Fluid properties	
Permittivity (F m^{-1})	7.08×10^{-10}
Electrical conductivity at 22 °C [μS cm^{-1}]	6.00
Temperature coefficient of conductivity ($°C^{-1}$)	0.022
Temperature difference across channel depth (K)	0.03
Working fluid at 55 °C	
Mean electrical conductivity (μS cm^{-1})	10.35
Dynamic viscosity (kg m^{-1} s^{-1})	4.89×10^{-4}
Density (kg m^{-3})	984.3
Geometry	
Electrode width (μm)	8
Electrode spacing (μm)	16
Pumping section length (cm)	1
Channel depth (μm)	50
Traveling-wave parameters	
Phases	3
Wavelength (μm)	72
Frequency (kHz)	122.1

of 54 °C (figure 5(*b*)), ΔT of 0.02–0.03 K is expected for free convection heat transfer coefficients in the range of 5–8 W m^{-2} K^{-1}. The majority of the dissipated heat is conducted through the lower branch of the resistance network (figure 10) as no special measures were taken to insulate the bottom of the channel, resulting in a relatively small temperature difference.

Using this estimated temperature difference and the operating parameters listed in table 5, we can compare the numerical model with the experimental data of figure 5 as shown in figure 11. Included in this figure are representative numerical cases at two voltages (20 V and 30 V) for $\Delta T =$ 0.03 K and the conditions outlined above. The average velocity values obtained experimentally and numerically are seen to be comparable in magnitude. Further, the measured rate of increase in velocity with applied voltage agrees well with the predicted rate. Using the same parameters in Melcher and Firebaugh's analytical model [15] as in the numerical model,

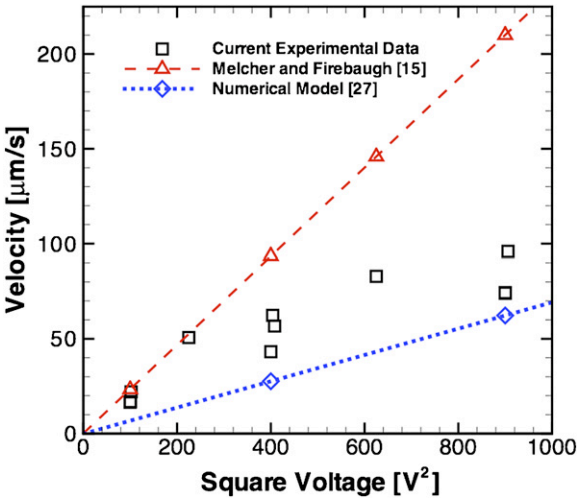

Figure 11. Comparison of the current experimentally obtained velocities as a function of the square of the applied voltage with Melcher and Firebaugh's analytical model [15] and a previous numerical model [27, 34].

it is apparent that the idealized analysis deviates from the measurements. Melcher and Firebaugh's model overpredicts the average velocity as compared to the experimental data and the current numerical model. Additionally, this discrepancy becomes more pronounced at higher applied voltages. This is likely due, in part, to the assumption of a perfect sinusoid voltage condition in [15] as discussed by Iverson *et al* [27].

Discrepancies between the numerical predictions and the experimental results can be attributed to a number of differences between the two.

- A time-varying voltage that switches as a step function between 0, $V/2$ and V is applied in the experiments. The voltage applied at the electrodes in the numerical model is defined using a continuously varying sinusoid in time. Thus, the electrodes in the model can take on voltages with magnitudes other than the three applied in the experiments. Other researchers have used overlapping rectangular pulses for the traveling wave and have noted differences between this method and single phase-shifted pulses and sinusoidal waves [35].
- The 1D resistance network approach used to estimate the very small temperature gradient, as well as deduction of a value for fluid temperature based on the measured exterior lower-wall temperature, involves approximations which can affect the predictions since the models are sensitive to these two parameters.
- The presence of a thin-film dielectric coating on top of the electrode array is not considered in the model, and would result in a decrease in the electric field experienced in the fluid, and thereby lead to the lower velocities noted in figure 11.
- Finally, we have neglected the effects of permittivity (ε) variation with temperature (T) in the aqueous solution used here since $\frac{1}{\varepsilon}\left(\frac{\partial \varepsilon}{\partial T}\right)$ is roughly 0.4% K^{-1} compared to the variation of conductivity (σ) with temperature, $\frac{1}{\sigma}\left(\frac{\partial \sigma}{\partial T}\right)$, which is roughly 2.2% K^{-1} [23, 24, 36].

Despite these differences between the numerical model and the experimental conditions, reasonable agreement is still observed between the two.

6. Heat removal capability

The heat transfer rate expected from the experimentally obtained velocities is now estimated, followed by a prediction of the heat removal capacity at higher flow rates. Beginning with the energy equation, the relative impact of convection and diffusion on the temperature profile in the channel can be estimated using an order of magnitude approach:

$$\rho c_p \vec{v} \cdot \vec{\nabla} T + \rho c_p \frac{\partial T}{\partial t} = k \vec{\nabla}^2 T + \sigma \vec{E}^2, \tag{2}$$

where ρ is density, c_p is specific heat, v is velocity, T is temperature, t is time, k is thermal conductivity, σ is electrical conductivity and E is electric field. Comparing the first and third terms in the energy equation above and using a dimensional analysis approach [30], we can estimate the relative significance of convection and diffusion by

$$\frac{\rho c_p v L}{k} \begin{cases} \ll 1 \text{ diffusion dominated} \\ = 1 \text{ comparable diffusion and convection} \\ \gg 1 \text{ convection dominated,} \end{cases} \tag{3}$$

where L is the channel depth. Considering the experiment with the 30 V input with an average measured velocity of 96 μm s^{-1}, the heat transfer is expected to be diffusion dominated since the velocities are small. Therefore, the upper branch of the resistance network shown in figure 10 can represent the expected heat removal rate dominated by diffusion. Following the 30 V example experimental case used to calculate a temperature difference of 0.03 K across the channel depth in section 5, a heat flux of 29 mW cm^{-2} (or a heat transfer rate of 14.5 mW for the 50 μm $\times$ 0.5 cm $\times$ 1 cm pump) is dissipated across the fluid layer.

The efficiency of a traveling-wave EHD device can be defined in a number of ways. However, if the desired outcome is heat removal, one possibility is to define it as

$$\eta = \frac{\text{desired output}}{\text{required input}} = \frac{q_{\text{out}}}{P_{\text{in}}}. \tag{4}$$

Here, q_{out} represents the amount of heat carried away by the induced flow and P_{in} represents the amount of power required by the device to drive the flow. Using the estimated cooling capacity of 14.5 mW above, for an input power of 635 mW (figure 9), the efficiency under these experimental conditions is 2.3%.

Forced convective cooling achieved with the EHD micropump can be enhanced by increasing the volume flow rate generated by the micropump, which can be achieved in a number of ways:

- increasing the traveling-wave peak voltage;
- selecting the appropriate traveling-wave frequency for peak velocity;
- increasing the electrode coverage area, decreasing the electrode spacing or reducing the traveling-wave wavelength;

- using higher order phase representations of the traveling wave and
- increasing the applied heat to achieve larger temperature differences across the channel depth.

The increase in flow rate due to many of these enhancements was computed in [27] (numerical case 7 in that work). Specifically, this case considered a five-phase device (6 μm electrodes, 6 μm spacing, 60 μm wavelength), a temperature difference of 10 K across the channel depth, a 200 V traveling-wave voltage, a channel height of 50 μm and a channel length of 1.0008 cm. This high temperature difference can be sustained across the fluid layer (see figure 10) for an input heat flux of 12 W cm^{-2} (or a heat transfer rate of 12 W for a 1 cm wide channel) with the bottom of the device being well insulated. The resulting volume flow rate for these conditions is 35.3 ml min^{-1} ($Re = 220$) at zero back pressure [27]. Flow rates of this magnitude would be convection dominated as indicated by equation (3). For this situation of laminar, fully developed flow with asymmetric heating between two parallel plates [37] (for a hydraulic diameter of 100 μm, $D_h = 2h_{\text{channel}}$ for parallel plates), it can be readily shown that the heat transfer coefficient would lie in the range of 24 000 to 32 340 W m^{-2} K depending on whether the top wall were insulated or losing all the heat as two bounding cases. Such high heat transfer coefficients are typical of microchannel cooling owing to their size. For a 10 K temperature difference across the channel and a heat transfer coefficient of 32 340 W m^{-2} K^{-1}, the estimated heat removal is approximately 34.5 W.

7. Conclusions

The appeal of EHD-induced flows is that they can be generated directly in the microchannel that houses the working fluid through integration of electrical networks using standard surface micromachining techniques. EHD exhibits a frequency-dependent fluid velocity and a maximum has been shown near or below the frequency based on the charge relaxation time constant. The average fluid velocity increases approximately linearly with the square of the applied voltage. Device self-heating is sufficient to produce the temperature difference in the channel depth required for traveling-wave induction EHD. For applications in which anisotropic heating is a part of the device environment (as in the case of electronics cooling), the energy for heating does not draw additional power for device operation and can increase the temperature gradient across the channel, resulting in increased fluid flow rates. An increase in fluid velocity by 49.6% was observed by adding 0.3 W of heat to the flow channel.

The heat removal mechanism at the experimentally obtained velocities is dominated by diffusion and limited to 14.5 mW for a 30 V applied voltage and a pump area of 0.5 cm^2. In order for EHD to find applications in electronics cooling, larger flow rates than those demonstrated in the present experiments are necessary. This may be achieved by exploiting the inherently large heat fluxes present in common IC packages to establish larger temperature gradients. Calculations based on a numerical analysis [27] of an optimized, microchannel-integrated EHD pump indicate that flow rates of 35.3 ml min^{-1} may be achieved by employing larger temperature differences and modifications to the traveling-wave design. Flow rates of this magnitude are capable of removing approximately 35 W of heat. Additionally, EHD offers the advantage of dynamic control of pumping on demand, such as for hotspot or transient thermal management.

Acknowledgments

The authors gratefully acknowledge funding and support from the National Science Foundation, the industry members of the Cooling Technologies Research Center, an NSF I/UCRC and the Indiana 21st Century Research and Technology Fund.

References

[1] Iverson B D and Garimella S V 2008 Recent advances in microscale pumping technologies: a review and evaluation *Microfluidics Nanofluidics* **5** 145–74
[2] Singhal V, Garimella S V and Raman A 2004 Microscale pumping technologies for microchannel cooling systems *Appl. Mech. Rev.* **57** 191–221
[3] Laser D J and Santiago J G 2004 A review of micropumps *J. Micromech. Microeng.* **14** 35–64
[4] Garimella S V and Singhal V 2004 Single-phase flow and heat transport and pumping considerations in microchannel heat sinks *Heat Transfer Eng.* **25** 15–25
[5] Garimella S V, Singhal V and Liu D 2006 On-chip thermal management with microchannel heat sinks and integrated micropumps *Proc. IEEE* **94** 1534–48
[6] Mahajan R, Chiu C-P and Chrysler G 2006 Cooling a microprocessor chip *Proc. IEEE* **94** 1476–86
[7] Andersson H and Van Den Berg A 2003 Microfluidic devices for cellomics: a review *Sensors Actuators* B **92** 315
[8] Whitesides G M and Stroock A D 2001 Flexible methods for microfluidics *Phys. Today* **54** 42–8
[9] Wolff A, Perch-Nielson I R, Larsen U D, Friis P, Goranovic G, Poulsen C R, Kutter J P and Telleman P 2003 Integrating advanced functionality in a microfabricated high-throughput fluorescent-activated cell sorter *Lab on a Chip* **3** 22–7
[10] Fu A Y, Spence C, Scherer A, Arnold F H and Quake S R 1999 A microfabricated fluorescence-activated cell sorter *Nat. Biotechnol.* **17** 1109–11
[11] Fu A Y, Chou H P, Spence C, Arnold F H and Quake S R 2002 An integrated microfabricated cell sorter *Anal. Chem.* **74** 2451–7
[12] Woias P 2005 Micropumps—past, progress and future prospects *Sensors Actuators* B **105** 28–38
[13] Nguyen N-T, Huang X and Chuan T K 2002 MEMS-micropumps: a review *J. Fluids Eng.* **124** 384–92
[14] Melcher J R 1966 Traveling-wave induced electroconvection *Phys. Fluids* **9** 1548–55
[15] Melcher J R and Firebaugh M S 1967 Traveling-wave bulk electroconvection induced across temperature gradient *Phys. Fluids* **10** 1178–85
[16] Seyed-Yagoobi J, Chato J C, Crowley J M and Krein P T 1989 Induction electrohydrodynamic pump in a vertical configuration: Part 1. Theory *J. Heat Transfer* **111** 664–9
[17] Seyed-Yagoobi J, Chato J C, Crowley J M and Krein P T 1989 Induction electrohydrodynamic pump in a vertical configuration: Part 2. Experimental study *J. Heat Transfer* **111** 670–4
[18] Seyed-Yagoobi J 2005 Electrohydrodynamic pumping of dielectric liquids *J. Electrost.* **63** 861–9
[19] Fuhr G, Hagedorn R, Muller T, Benecke W and Wagner B 1992 Microfabricated electrohydrodynamic (EHD) pumps

for liquids of higher conductivity *J. Microelectromech. Syst.* **1** 141–6
[20] Choi J W and Kim Y K 1995 Micro electrohydrodynamic pump driven by traveling electric fields *IEEE Industry Applications Conference, 30th IAS Annual Meeting (Orlando, FL, 8–12 October 1995* pp 1480–4
[21] Crowley J M, Wright G S and Chato J C 1990 Selecting a working fluid to increase the efficiency and flow rate of an EHD pump *IEEE Trans. Ind. Appl.* **26** 42–9
[22] Fuhr G, Schnelle T and Wagner B 1994 Travelling wave-driven microfabricated electrohydrodynamic pumps for liquids *J. Micromech. Microeng.* **4** 217–26
[23] Perch-Nielsen I R, Green N G and Wolff A 2004 Numerical simulation of travelling wave induced electrothermal fluid flow *J. Phys. D: Appl. Phys.* **37** 2323–30
[24] Green N G, Ramos A, Gonzalez A, Castellanos A and Morgan H 2001 Electrothermally induced fluid flow on microelectrodes *J. Electrost.* **53** 71–87
[25] Felten M, Geggier P, Jager M and Duschl C 2006 Controlling electrohydrodynamic pumping in microchannels through defined temperature fields *Phys. Fluids* **18** 051707
[26] Singhal V and Garimella S V 2007 Induction electrohydrodynamics micropump for high heat flux cooling *Sensors Actuators* A **134** 650–9
[27] Iverson B D, Cremaschi L and Garimella S V 2009 Effects of discrete-electrode configuration on traveling-wave electrohydrodynamic pumping *Microfluidics Nanofluidics* **6** 221–30
[28] Schlitz D 2004 Microscale Ion Driven Airflow *PhD Thesis* School of Mechanical Engineering, Purdue University, West Lafayette, IN
[29] Serway R A, Moses C J and Moyer C A 2005 *Modern Physics* (Belmont, MA: Brooks Cole)
[30] Ramos A, Morgan H, Green N G and Castellanos A 1998 AC electrokinetics: a review of forces in microelectrode structures *J. Phys. D: Appl. Phys.* **31** 2338–53
[31] Wereley S T, Gui L and Meinhart C D 2002 Advanced algorithms for microscale particle image velocimetry *AIAA J.* **40** 1047–55
[32] Crowley J M 1980 The efficiency of electrohydrodynamic pumps in the attraction mode *J. Electrost.* **8** 171–81
[33] Fluent 1998 FIDAP, Vers. 8.7.4, finite element software
[34] Singhal V and Garimella S V 2005 A novel valveless micropump with electrohydrodynamic enhancement for high heat flux cooling *IEEE Trans. Adv. Packag.* **28** 216–30
[35] Fuhr G, Hagedorn R, Muller T, Benecke W and Wagner B 1992 Pumping of water solutions in microfabricated electrohydrodynamic systems *Proc. IEEE Micro Electromechanical Systems Workshop (Travemuende, Germany, 4–7 February 1992* pp 25–30
[36] Lide D 2001 *CRC Handbook of Chemistry and Physics* (New York: CRC Press)
[37] Kays W M and Crawford M E 1993 *Convective Heat and Mass Transfer* (New York: McGraw-Hill)